ARTICLES
PUBLISHED ONLINE: 10 NOVEMBER 2014 | DOI: 10.1038/NPHYS3140
nature physics

Observation of topological surface state quantum Hall effect in an intrinsic three-dimensional topological insulator

Yang Xu[1,2], Ireneusz Miotkowski[1], Chang Liu[3,4], Jifa Tian[1,2], Hyoungdo Nam[5], Nasser Alidoust[3,4], Jiuning Hu[2,6], Chih-Kang Shih[5], M. Zahid Hasan[3,4] and Yong P. Chen[1,2,6]*

A three-dimensional (3D) topological insulator (TI) is a quantum state of matter with a gapped insulating bulk yet a conducting surface hosting topologically protected gapless surface states. One of the most distinct electronic transport signatures predicted for such topological surface states (TSS) is a well-defined half-integer quantum Hall effect (QHE) in a magnetic field, where the surface Hall conductivities become quantized in units of (1/2)e^2/h (e being the electron charge, h the Planck constant) concomitant with vanishing resistance. Here, we observe a well-developed QHE arising from TSS in an intrinsic TI of BiSbTeSe$_2$. Our samples exhibit surface-dominated conduction even close to room temperature, whereas the bulk conduction is negligible. At low temperatures and high magnetic fields perpendicular to the top and bottom surfaces, we observe well-developed integer quantized Hall plateaux, where the two parallel surfaces each contribute a half-integer e^2/h quantized Hall conductance, accompanied by vanishing longitudinal resistance. When the bottom surface is gated to match the top surface in carrier density, only odd integer QH plateaux are observed, representing a half-integer QHE of two degenerate Dirac gases. This system provides an excellent platform to pursue a plethora of exotic physics and novel device applications predicted for TIs, ranging from magnetic monopoles and Majorana particles to dissipationless electronics and fault-tolerant quantum computers.

The integer quantum Hall effect (QHE) in a 2D electron system (2DES) under a perpendicular magnetic field is the first example of a topological quantum state[1–5]. In the QHE, the Hall conductivity (σ_{xy}, which is equal to the Hall conductance) is quantized at $\nu e^2/h$, where the integer ν, representing the number of filled Landau levels (LLs), is a topological invariant independent of material details[3,4]. The quantized σ_{xy} that measures this topological invariant is accompanied by vanishing longitudinal resistance (R_{xx}) due to dissipationless transport carried by ballistic chiral edge states, whereas the bulk of the sample is insulating[2]. Such quantum Hall (QH) systems have become a major paradigm in condensed matter physics, with important applications such as resistance metrology and measurements of fundamental constants[1,5]. In the past few years, it has been realized that the QHE is just one member of a much larger family of topologically distinctive quantum states, some examples of which include the quantum spin Hall (QSH) effect (also known as the '2D topological insulator') and (3D) TIs (refs 6,7), both preserving the time reversal (TR) symmetry and induced by strong spin–orbit coupling rather than external magnetic fields (in contrast to the QHE). Now realized or predicted in a large number of materials, TIs with their characteristic spin-helical Dirac fermion TSS have attracted intense interest for the rich physics and applications they promise.

Theories suggest that breaking the TR symmetry in TIs, either by internal magnetic doping or external magnetic fields, could result in a half-quantized surface Hall conductance ($e^2/2h$), directly reflecting the topologically nontrivial nature of the underlying quantum state[8,9]. Such a half-quantized Hall conductance also has connections with topological magnetoelectric effect (TME, formally analogous to an 'axionic electrodynamics' first proposed in a particle physics context), which could lead to other novel physics such as quantized electromagnetic and optical responses (for example, Kerr rotation)[7,9]. Recent experiments have realized the predicted[10,11] quantum anomalous Hall effect (QAHE, with σ_{xy} quantized at $2 \times e^2/2h = e^2/h$ in zero external magnetic field, with the multiplicative factor of 2 arising from two surfaces) in magnetically doped TI films[12]. Although experiments under external magnetic fields have so far reported Shubnikov–de Hass (SdH) oscillations (commonly considered a precursor for the QHE (ref. 5)) from TSS in various TI materials[13–17], and even developing QHE in strained HgTe TI films[18,19], a fully developed TSS QHE characterized by well-quantized R_{xy} plateaux and vanishing (dissipationless) R_{xx} with a truly insulating bulk has been difficult to achieve.

In this work, we report observations of a well-developed TSS QHE in BiSbTeSe$_2$, an intrinsic TI material where the bulk is highly insulating with negligible conductance. The slab-shaped samples with parallel top and bottom surfaces in a quasi-Hall-bar configuration under high magnetic fields exhibit vanishing R_{xx} with quantized $\sigma_{xy} = \nu e^2/h$, where ν is an integer equal to

---

[1]Department of Physics and Astronomy, Purdue University, West Lafayette, Indiana 47907, USA. [2]Birck Nanotechnology Center, Purdue University, West Lafayette, Indiana 47907, USA. [3]Joseph Henry Laboratories, Department of Physics, Princeton University, Princeton, New Jersey 08544, USA. [4]Princeton Institute for Science and Technology of Materials, Princeton University, Princeton, New Jersey 08544, USA. [5]Department of Physics, University of Texas at Austin, Austin, Texas 78712, USA. [6]School of Electrical and Computer Engineering, Purdue University, West Lafayette, Indiana 47907, USA.
*e-mail: yongchen@purdue.edu

$(N_t + N_b + 1) = (N_t + 1/2) + (N_b + 1/2)$, with $N_{t(b)}$ being the corresponding LL index for the top (bottom) surface (each surface filling half-integer LLs). The quantized σ_{xy} is insensitive to the sample thickness and can be understood as the sum of two half-integer quantized Hall conductances (QHC) of the two parallel conducting surfaces, even though the individual surface Hall conductance cannot be directly measured.

Materials

Commonly studied 'prototype' 3D TIs, nearly-stoichiometric Bi_2Se_3, Bi_2Te_3 and Sb_2Te_3, often have significant bulk conductance due to naturally-occurring defects and the resulting unintentional bulk doping[13,14,20,21]. It has been a challenge to eliminate the bulk conduction and reveal the transport signature of the Dirac carriers in TSS (refs 13,14,21,22). Recently, ternary and quaternary tetradymite TI materials such as Bi_2Te_2Se and $Bi_{2-x}Sb_xTe_{3-y}Se_y$ have been found to exhibit large bulk resistivity and more intrinsic TI behaviours[15,16,23–25]. We have grown (see Methods) high-quality single crystals of Bi–Sb–Te–Se solid solution with a Bi:Sb:Te:Se ratio close to 1:1:1:2, referred to as $BiSbTeSe_2$ (or simply abbreviated as BSTS) in this paper. Various material characterizations have been performed on our BSTS crystals (see Supplementary Figs 1–3), including the confirmation of the TI nature by angle-resolved photoemission spectroscopy (ARPES, Supplementary Fig. 2) revealing the Dirac TSS band with a well-isolated Dirac point (DP) located close to the Fermi level (E_F), and measurement of a large bulk bandgap of ~0.3 eV (Supplementary Fig. 3, by scanning tunnelling spectroscopy), all in good agreement with previous measurements in this material system[23,26]. Hall coefficients measured in relatively thick crystals (Supplementary Fig. 4) at low temperature indicate the bulk carrier density to be negligibly small (of the order of or below the extracted effective 3D carrier density of $\sim 10^{15}\,\mathrm{cm}^{-3}$ that mostly come from the surface) and at least an order of magnitude lower than the lowest value reported previously[13,16,17,25]. Typical surface Hall mobilities range from 1,000 to 3,000 $\mathrm{cm}^2\,\mathrm{V}^{-1}\,\mathrm{s}^{-1}$ in our samples.

Results and analysis

We first discuss transport measurements performed at zero magnetic field ($B = 0$ T) on BSTS samples with various thicknesses (t). Figure 1a shows the temperature (T) dependence of the sheet resistance R_{sh} in five selected samples. The thicker samples (for example, $t = 37\,\mu\mathrm{m}$) exhibit an insulating behaviour (attributed to the bulk) at high T and a saturating and weakly metallic behaviour (attributed to the residual metallic surface conduction after bulk carriers freeze out) at low T. As the thickness (and, thus, the bulk portion) is reduced (for example, $t = 160$ and 480 nm), the bulk insulating behaviour weakens and moves to higher T, whereas the T range for the low-T metallic conduction expands. For the thinnest samples ($t = 20$ nm), R_{sh} is relatively insensitive to T and metallic over the entire T range measured. We also note that whereas R_{sh} (attributed to the bulk) at high T ($\gtrsim$250 K) is strongly dependent on thickness (from <10 Ω to >2 kΩ), R_{sh} (attributed to the surface) at low T (<50 K) reaches comparable values (a few kΩ) for all the samples despite the three orders of magnitude variation in their thickness. This contrasting behaviour is more clearly seen in Fig. 1b, where we plot both R_{sh} (left axis) as well as the corresponding 3D resistivity ρ_{3D} ($= R_{sh}t$) as functions of thickness (t, for all measured samples) at $T = 2$ K and 290 K (room temperature). At low $T = 2$ K, R_{sh} is insensitive to the thickness (ranging from 20 nm to 52 μm), consistent with the conduction being dominated by the 2D surface (thus, independent with thickness) with little contribution from the bulk. In this case, the resistivity (ρ_{3D}) normally used to characterize a 3D conducting material is no longer well defined (and becomes strongly dependent on thickness, as seen in our data, with ρ_{3D} approximately proportional to t, as indicated by the dotted line). On the other hand, at high $T = 290$ K and for samples thicker than ~100 nm, the observed behaviour becomes well described by that expected of a 3D bulk conductor ($R_{sh} \propto 1/t$ and $\rho_{3D} \sim$ constant, highlighted by the dashed line and horizontal band respectively), consistent with the conduction now being dominated by the thermally activated carriers in the bulk. Interestingly, even at such high T (room temperature), the thinner samples ($t < 100$ nm) still deviate from the 3D behaviour, indicating a substantial conduction contribution from the surface (see also Supplementary Fig. 5).

To more quantitatively extract the surface contribution to the total conductance (G^{tot}), we fit our $R_{sh}(T)$ data to a simple model used in ref. 27, where the total (sheet) conductance $G^{tot}(T) = 1/R_{sh}(T)$ is the parallel sum of a thermally activated bulk conductance $G_b(T) = t(\rho_{b0}e^{\Delta/kT})^{-1}$, where k is the Boltzmann constant with the fitting parameters being ρ_{b0}, the high temperature bulk resistivity, and Δ, the activation energy, and a metallic surface conductance $G^{sur}(T) = (R_{sh0} + AT)^{-1}$, where the fitting parameters are R_{sh0}, representing a low-T residual resistance (due to impurity scattering), and A, reflecting the electron–phonon scattering[27,28]. We find that this model gives reasonable good fits to most of our data, and extract the surface conductance G^{sur} for samples with different thickness (see Supplementary Fig. 6 for more details). Figure 1c shows the ratio (G^{sur}/G^{tot}) between the fitted G^{sur} and the measured total conductance G^{tot} as a function of thickness (t) at three representative temperatures. At low T (50 K or below), the surface contribution to the total conductance is nearly 100% for all the samples (with thickness from <100 nm to >10 μm). Remarkably, in thinner samples ($t < 100$ nm) the surface conduction can exceed the bulk conduction, with $G^{sur}/G^{tot} > 60\%$ even at room temperature ($T = 290$ K). For each fitting parameter, the values for all samples (with a wide range of thicknesses) are found to be of a similar order of magnitude (Supplementary Fig. 6, given the moderate density and mobility variations expected between different samples). The averaged fitting parameters (between all samples) $\rho_{b0} = (3.5 \pm 0.8) \times 10^{-3}\,\Omega\,\mathrm{cm}$, $\Delta = 57 \pm 4$ meV, $R_{sh0} = 2.0 \pm 0.3\,\mathrm{k}\Omega$, $A = 6 \pm 2\,\Omega\,\mathrm{K}^{-1}$ can be taken as representative material parameters for our BSTS to predict G^{sur}/G^{tot} for any given thickness and temperature, as shown in the 2D colour plot in Fig. 1d. We see that surface-dominant transport with ($G^{sur}/G^{tot} > 80\%$) can be achieved at moderately low T (<50 K) for samples up to macroscopic thicknesses of 1 mm, or in thin (tens of nm) samples up to room temperature (300 K) in this material system. The extracted bulk thermal activation energy Δ is greater than $2kT$ for $T = 300$ K, which enables surface-dominant transport at room temperature. We also note that Δ is much smaller than the bulk band gap of ~300 meV. This has been noted in previous measurements in similar materials[17], and may be a result of impurity states in the bulk gap in the compensation-doped sample (while spatial variation in the doping can further reduce the observed Δ)[29].

Measurements of the quantum Hall effect (QHE) were performed in two samples ('A' and 'B') with intermediate $t = 160$ nm and 80 nm, respectively. They are thick enough such that our Si/SiO_2 backgate can be used to independently[22] tune the bottom surface carrier density n_b without affecting the top surface density n_t (see Fig. 2a inset for the device schematic), yet still thin (and small) enough to ensure negligible bulk and side surface conduction and a high degree of sample uniformity. Figure 2a shows a representative backgate modulation of R_{xx} (field effect) measured at $T = 0.35$ K without an external magnetic field in sample A (image shown in Fig. 2b inset). The peak in R_{xx} at $V_D \sim -60$ V is identified as the charge neutrality point (DP) of the bottom surface, whose carriers change from electrons at higher V_{bg} to holes at lower V_{bg}. Repeated gate sweeps can have a slight hysteresis (of several volts). The ungated surfaces (both bottom surface, as seen by the field effect, and top surface, see discussions below) are generally found to be n-type

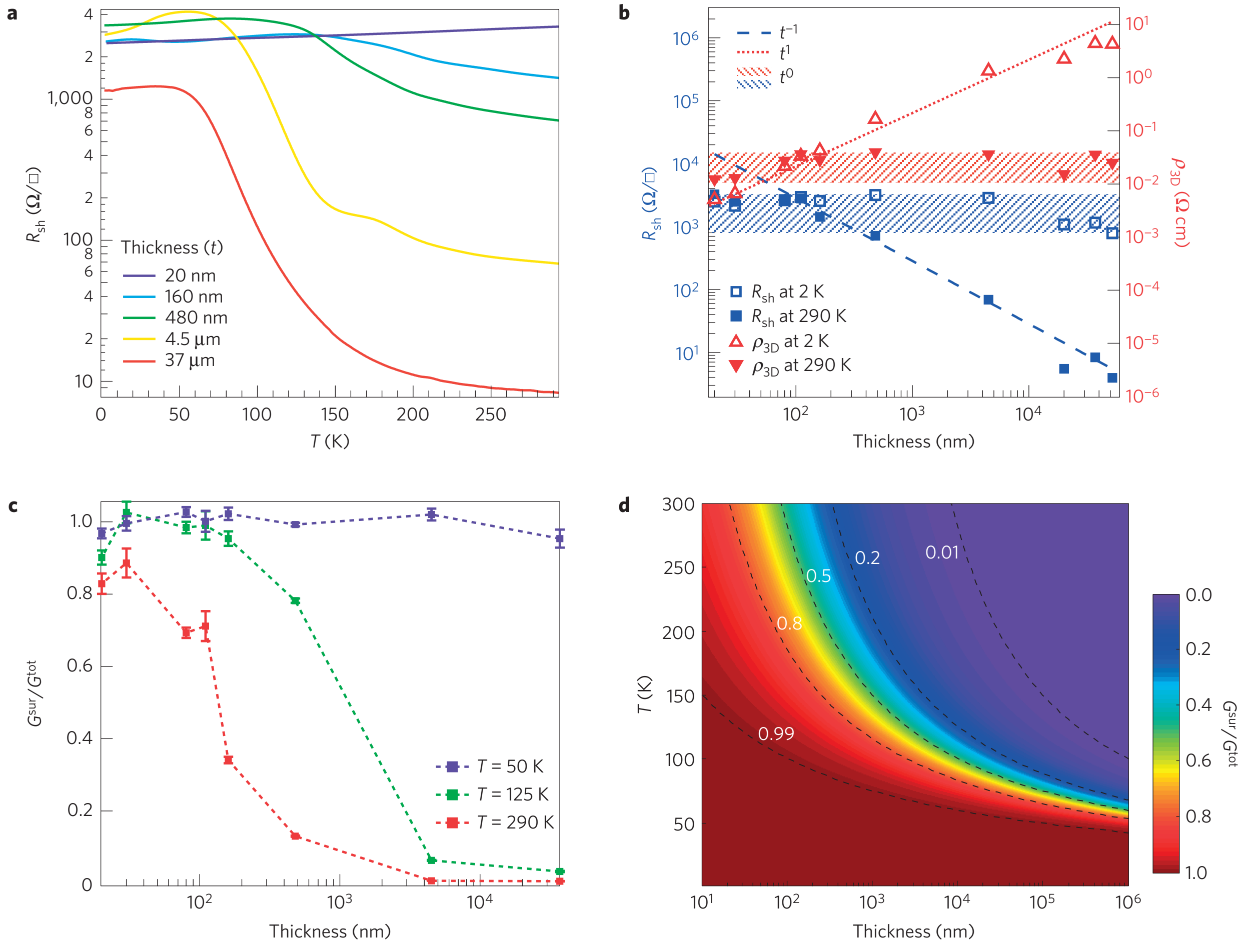

Figure 1 | Surface versus bulk conduction in BSTS. a, Sheet resistance (R_{sh}) measured at zero magnetic field versus temperature (T) in five devices with different thicknesses. **b**, R_{sh} and 3D resistivity ρ_{3D} as functions of sample thickness at two typical temperatures. At $T = 2$ K, the sheet resistance exhibits a 2D behaviour (relatively insensitive to the thickness, highlighted by the blue horizontal band). The dashed line and red horizontal band represent expected behaviours for R_{sh} and ρ_{3D} of a 3D bulk conductor (our data at 290 K exhibited such 3D behaviour for samples thicker than $\gtrsim$100 nm). **c**, Surface to total conductance ratio (G^{sur}/G^{tot}) as a function of the sample thickness at three representative temperatures. Here G^{tot} is the measured conductance and G^{sur} is extracted from fitting the measured R_{sh} versus T (see text and Supplementary Fig. 6 for details, the few G^{sur}/G^{tot} exceeding unity by a few per cent is a result of the fit slightly overestimating the measured data). **d**, Predicted G^{sur}/G^{tot} (shown in colour scale) for our BSTS as a function of temperature and sample thickness. Here G^{sur} and G^{tot} are calculated based on the bulk and surface conductivities averaged from multiple measured devices (see text and Supplementary Fig. 6 for details). Black dashed curves are contours for a few G^{sur}/G^{tot} values.

(with electron carriers) in the exfoliated thin flakes used in our QHE measurements.

Figure 2b presents the longitudinal resistance R_{xx} ($= V_{23}/I_{14}$, where subscripts label voltage (V) or current (I) leads shown in the inset) and Hall resistance R_{xy} ($= V_{53}/I_{14}$) as functions of the backgate voltage V_{bg}, measured at $T = 0.35$ K in sample A and with a magnetic field $B = 31$ T applied perpendicular to the top and bottom surfaces. At the electron side ($V_{bg} > -60$ V) of the bottom surface (same carrier type as the ungated top surface), we observe well-defined quantized plateaux in R_{xy}, with values $\sim h/e^2 \sim 25.8$ kΩ and $\sim h/(2e^2) \sim 12.9$ kΩ, accompanied by vanishing R_{xx}, over broad ranges in V_{bg} around -45 V and -20 V respectively. These are the hallmarks of a well-developed QHE, associated with total (top + bottom surfaces) Landau filling factors $\nu = 1$ and 2 respectively (see more discussions below). In addition, we also observe a developing R_{xy} plateau $\sim h/(3e^2)$, accompanied by a minimum in R_{xx}. To gain more insights into the QHE, we perform tensor inversion to extract the 2D longitudinal and Hall conductivities σ_{xx} and σ_{xy}, shown in Fig. 2c in units of e^2/h. We again observe quantized (and developing) plateaux in σ_{xy} at $\nu e^2/h$ with integer $\nu = 1$, 2 (and 3), concomitant with vanishing σ_{xx} (minimum in σ_{xx}). Such integer quantized Hall conductivities (QHC) measured can be understood as the sum of a half-integer QHC from the top surface (fixed at $(1/2)e^2/h$ at $B = 31$ T) and another half-integer QHC from the bottom surface (at $\nu_b e^2/h$ with $\nu_b = 1/2$, 3/2, and 5/2 and so on, depending on the n_b tuned by the back gate). In other words, the observed QHC $\sigma_{xy}^{\text{total}} = \nu e^2/h = \sigma_{xy}^{\text{top}} + \sigma_{xy}^{\text{bottom}} = (\nu_t + \nu_b)e^2/h = (N_t + N_b + 1)e^2/h$, with top (bottom) surface QHC $\sigma_{xy}^{\text{top(bottom)}} = \nu_{t(b)}e^2/h = (N_{t(b)} + 1/2)e^2/h$, where $\nu_{t(b)} = N_{t(b)} + 1/2$ and $N_{t(b)}$ are the Landau filling factor and Landau level index of the top (bottom) surface corresponding to the QH state (in our case $\nu_t = 1/2$ and $N_t = 0$, thus $\sigma_{xy}^{\text{top}} = (1/2)e^2/h$), even though the individual (half-integer) QHC of each surface cannot be directly measured in the experiment (where we always measure the total Hall conductance of the two parallel conducting surfaces). Such a half-integer QHE reflecting the contribution in units of half quantum conductance ($e^2/2h$) from each surface is the hallmark of the topological surface state QHE unique to 3D TI, and is the main focus of this paper. Also of interest is the observation when the bottom surface is gated ($V_{bg} < -60$ V) to the hole side to have the opposite carrier type to that of the top surface, that weakly developed plateau-like features appear in σ_{xy} around $0e^2/h$ and $-1e^2/h$, accompanied by inflection

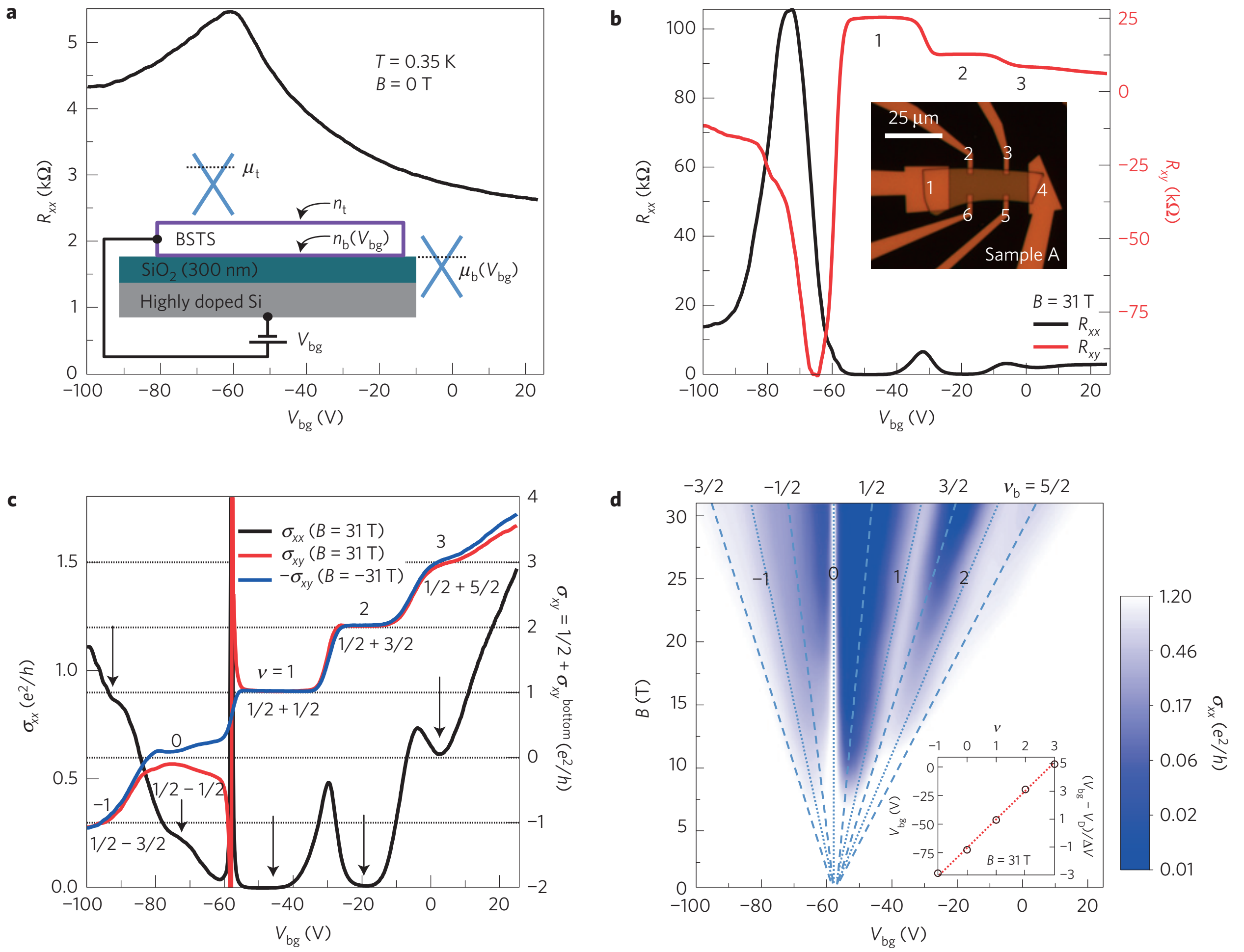

Figure 2 | Electric field effect and gate-tuned quantum Hall effect (QHE) in BSTS. a, Representative electric field effect curve, showing the resistance R_{xx} measured as a function of V_{bg} in Sample A (a 160-nm-thick exfoliated BSTS flake). Inset is the device schematic, where the doped Si substrate (with 300 nm SiO_2 overlayer) is used as a backgate (V_{bg} denotes the gate voltage applied) to tune the carrier density n_b (and thus the chemical potential μ_b) of the bottom surface of the BSTS. Also depicted are the Dirac surface state bands for top and bottom surfaces, respectively. **b**, Longitudinal resistance (R_{xx}) and Hall resistance (R_{xy}) versus backgate voltage (V_{bg}) measured at $B = 31$ T in Sample A (inset shows an optical microscope image of the device) at 0.35 K. **c**, Extracted 2D longitudinal and Hall conductivities (σ_{xx} and σ_{xy} at 31 T along with $-\sigma_{xy}$ at −31 T), in units of e^2/h. Plateaus observed in R_{xy} (at values of $h/\nu e^2$) and σ_{xy} (at $\nu e^2/h$) are labelled by the corresponding total Landau filling factors (ν, which are integers, with corresponding sum of top and bottom surface half-integer fillings also labelled in Fig. 2c) of the quantum Hall states. Arrows mark the minima or inflection in σ_{xx}. **d**, A 2D colour plot showing σ_{xx} (colour scale) as a function of magnetic field (B) and back gate voltage (V_{bg}) measured at 0.35 K in sample A. A series of σ_{xx} versus V_{bg} curves (measured in steps of 2 T) are interpolated to generate this 2D plot. Dashed and dotted lines correspond to half-integer and integer Landau filling factors (marked) for the bottom surface, respectively. Inset: the V_{bg} positions for minima in σ_{xx} (left axis) and $(V_{bg} - V_D)/\Delta V$ (right axis) as a function of ν at 31 T, where ΔV is half the averaged V_{bg} separation between two consecutive Landau levels.

points in σ_{xx} (but no obvious corresponding features in R_{xx} and R_{xy}, Fig. 2b). It remains to be understood whether these features may relate to some underlying QH states with $(\nu_t, \nu_b) = (1/2, -1/2)$ and $(1/2, -3/2)$, respectively. We also reproduce all the observed QH states under $B = -31$ T (Supplementary Fig. 7), highlighted by the $-\sigma_{xy}$ shown in Fig. 2c, exhibiting a more 'smooth' transition between the '$1/2 - 1/2$' feature and '$1/2 + 1/2$' plateau (the detailed 'transition' behaviours in magnetotransport near the bottom surface DP ($\nu_b \sim 0$) are dependent on the direction of B and not the focus of this discussion, see also Supplementary Fig. 8).

We further studied $\sigma_{xx}(V_{bg})$ at a series of magnetic field values (B), and found quantum Hall features can be observed down to $B = 13$ T (data traces of σ_{xx} and σ_{xy} as well as R_{xx} and R_{xy} are shown in Supplementary Fig. 9). Figure 2d plots σ_{xx} (colour scale) as functions of both B and V_{bg}. Dashed lines trace the gate voltage (V_{bg}) positions for the observed QH minima in σ_{xx} and are labelled with the corresponding half-integer fillings (ν_b) of the bottom surface LL. When extrapolated to $B = 0$ T, these lines converge to ~ -58 V, the bottom surface DP (V_D). Dotted lines trace the maxima in σ_{xx}, labelled with the corresponding integer ν_b, also extrapolate and converge to the same DP. The odd integer ratio (−3:−1:1:3:5) in the V_{bg} positions for the QH minima in σ_{xx} as measured away from the DP ($V_{bg} - V_D$, proportional to n_b), exemplified in the inset for the five QH minima in σ_{xx} at $B = 31$ T (corresponding to the intercepts of dashed lines on the top axis in Fig. 2d), is in contrast to the QHE for a conventional 2DES, where the density (filling factor) ratio for successive QHE states (σ_{xx} minima) would be consecutive integers. This half-integer shift in our data (integer/half-integer fillings for maxima/minima) is a consequence of the unique zeroth LL being shared equally between Dirac electrons and holes, and a manifestation of the Berry's phase π associated with spin-helical carriers of TSS. It is known that σ_{xx} peaks when the gate-tunable chemical potential (μ_b) passes through the centre of the last-filled LLs, where the density of state (DOS) peaks and underlying

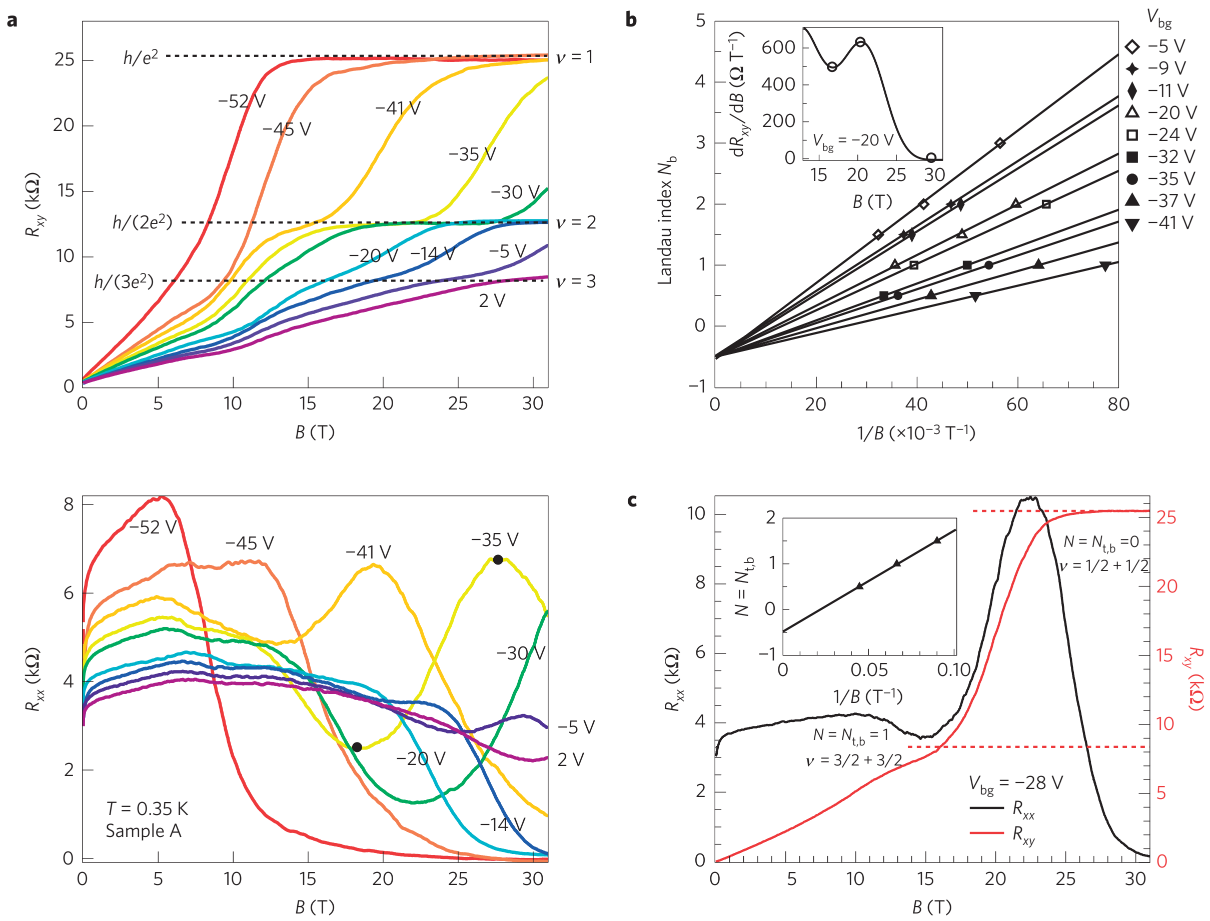

Figure 3 | Magnetic field tuned QHE. a, R_{xx} (bottom) and R_{xy} (top) as functions of B at various V_{bg} values. Several observed quantum Hall plateaus are marked by dashed lines with corresponding total Landau filling factors ν (top). **b**, Landau fan diagram for the bottom surface for various different V_{bg} values. Data shown with filled markers are extracted from $R_{xx}(B)$ whereas those shown with open markers are from the derivative of $R_{xy}(B)$ (an example at $V_{bg} = -20$ V is shown in the inset). Examples of extracted data points are marked in the inset and the R_{xx} trace for $V_{bg} = -35$ V in **a**. Only data with $B \gtrsim 13$ T (where the top surface is at its zeroth LL) are used. Lines denote linear fits with N_b-axis intercepts $\sim -1/2$ for all datasets. **c**, Measurements were performed in a different cool-down with different carrier densities. Magnetic field (B) dependence of R_{xx} and R_{xy} measured at $V_{bg} = -28$ V, where n_b is tuned to match n_t (top surface carrier density) such that the LL index $N = N_t = N_b$. Inset shows a LL fan diagram, where integers N (half-integers $N + 1/2$) are assigned to index minima (maxima) in R_{xx} oscillations. A linear fit gives the intercept −0.5 on the N-axis. All data in **a**–**c** are measured in sample A at 0.35 K.

state may become delocalized[2,5]. The prominent central peak (the central line with $\nu_b = 0$, non-dispersive with B) at the DP in our σ_{xx} data represents the zeroth LL, which is fixed at zero energy and non-dispersive with B, and a hallmark of Dirac fermions.

We also measure QHE by sweeping the magnetic field (B) at fixed carrier densities (V_{bg}). Figure 3a shows R_{xy} and R_{xx} measured versus B at $T = 0.35$ K in sample A for various V_{bg} values. The $R_{xy}(B)$ trace for $V_{bg} = -52$ V (close to the bottom surface DP) exhibits a wide quantized plateau $\sim h/e^2$ for $B \gtrsim 13$ T, indicating both surfaces are in the $1/2(e^2/h)$ QH state (zeroth LL, $N_t = N_b = 0$, $\nu = 1/2 + 1/2 = 1$). When V_{bg} is increased to −41 V, the higher n_b shifts the $\nu_b = 1/2$ ($N_b = 0$) QH state of the bottom surface and, thus, the observed $h/e^2 (\nu = 1)$ plateau to higher B. Meanwhile, another QH plateau develops at $h/2e^2$ at lower $B \sim 15$ T (but still $\gtrsim 13$ T with $N_t = 0$), corresponding to $N_b = 1$, $\nu = \nu_t + \nu_b = 1/2 + 3/2 = 2$. This QH state also shifts to higher B as V_{bg} increases (−35 V, −30 V and −20 V). Further increasing V_{bg} to −14 V, −5 V and 2 V, yet another QH plateau develops at $h/3e^2$, now corresponding to $N_t = 0$, $N_b = 2$, $\nu = \nu_t + \nu_b = 1/2 + 5/2 = 3$. All these QH plateaus are accompanied by vanishing R_{xx} or dips in R_{xx}, with each QH state generally better developed at higher B (reflecting the larger LL energy gap). From the evolution of the QH states seen in Fig. 3a for $B \gtrsim 13$ T, we can extract the bottom surface LL index N_b (note N_t is fixed at 0) and perform the standard fan diagram analysis (Fig. 3b, showing N_b versus $1/B$), where integer/half-integer N_b is assigned to the minima/maxima in R_{xx} (or alternatively in dR_{xy}/dB, with an example shown in Fig. 3b inset). We find N_b versus $1/B$ (exhibiting good linear fit, see more analysis in Supplementary Fig. 10) extrapolates (in the limit of $1/B \to 0$) to an N-axis intercept of $\sim -1/2$ for all V_{bg} values studied. Such a 1/2-intercept in LL index is again a hallmark of Dirac fermions and underlies the half-integer QHE.

Also of interest in Fig. 3a is the trace measured with $V_{bg} = -45$ V, which is near the centre of the $\nu = 1$ QH plateau in R_{xy} (V_{bg}) in Fig. 2b, with estimated $n_b \sim n_t$. With the two surface densities nearly matched, R_{xy} exhibits a developing QH state $\sim h/3e^2$ (corresponding to $N_t = N_b = 1$, $\nu = 3/2 + 3/2 = 3$) at lower $B \sim 10$ T, in addition to the h/e^2 QH plateau ($N_t = N_b = 0$, $\nu = 1/2 + 1/2 = 1$) at high B. These two QH states can be considered as belonging to a half-integer QHE series of $\nu = g(N + 1/2)$, where N is the common LL index (=0 and 1 in our case) and $g = 2$ represents the two (nearly degenerate) surfaces. Another example of such a QHE with matched surface densities is shown in Fig. 3c, measured with $V_{bg} = -28$ V in a different cool-down of Sample A, that resulted in higher as-cooled surface carrier densities. The QH plateau near $h/(3e^2)$ appears at higher $B \sim 15$ T and is better developed, accompanied by a clear

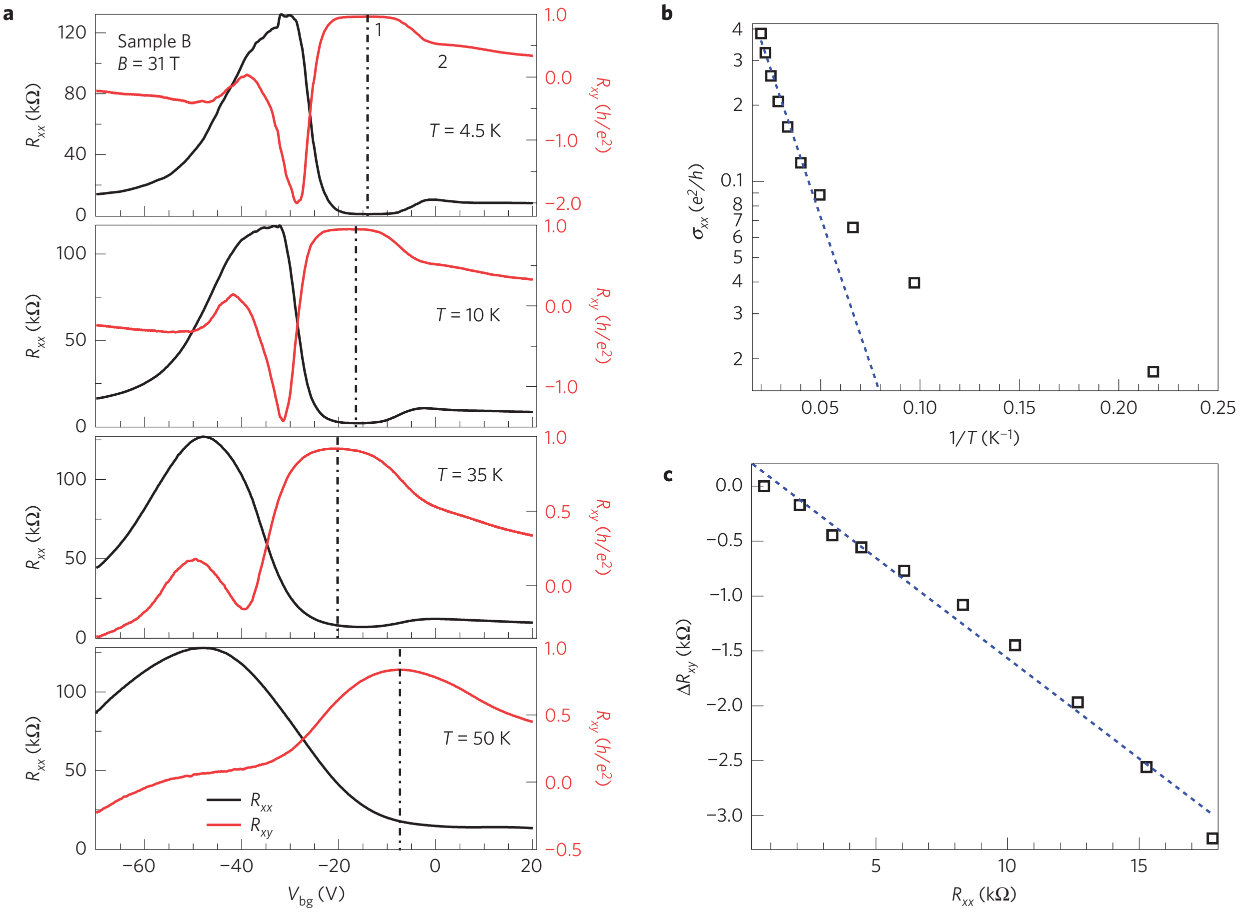

Figure 4 | QHE measured in a different sample and temperature dependence. Measurements were performed in Sample B, an 80-nm-thick exfoliated BSTS flake. **a**, V_{bg}-dependent R_{xx} and R_{xy} measured at $B=31$ T and four different temperatures (4.5 K, 10 K, 35 K and 50 K). Vertical dot-dashed lines indicate the position of the QH state at total filling factor $\nu=1$. **b**, σ_{xx} (log scale) as a function of inverse temperature ($1/T$) at $\nu=1$. Blue dashed line indicates a fit at higher temperature with $\sigma_{xx}\propto\exp(-E_0/kT)$. **c**, ΔR_{xy} versus R_{xx} at $\nu=1$. Blue dashed line indicates a linear fit.

minimum in R_{xx}. The conspicuous absence of the $\nu=2$ QH state is again consistent with the 'half-integer' QHE expected for two-flavour (representing two surfaces) Dirac fermions at odd-integer total filling $\nu=2(N+1/2)=2N+1$, with the LL index $N=N_t=N_b$. The inset of Fig. 3c shows the corresponding Landau fan diagram for the common LL index $N=N_{t,b}$, with the linear fit again yielding the expected intercept of $N\sim-0.5$ for the Dirac fermions in the high-B limit (thus $\nu=2(N+1/2)\to 0$). The gate-tuned QHE from this cool down can be found in Supplementary Fig. 11.

Figure 4a shows the backgate-tuned QHE (R_{xx} and R_{xy} versus V_{bg}) measured at fixed $B=31$ T in Sample B (thickness $t=80$ nm) at different temperatures (T). At low T (4.5 K), we observe QH states corresponding to $\nu=1$ (well-developed) and $\nu=2$ (developing), interpreted (similarly to Sample A, Fig. 2) as $\nu_t+\nu_b=1/2+1/2$ and $1/2+3/2$ respectively. The insensitivity of the quantization values to the sample thickness (changing by factor of two between samples A and B) confirms that the observed QHE arises from the surface of the intrinsic TI, and is not related to the 'bulk' QHE observed previously (in highly bulk-doped Bi_2Se_3, attributed to electronic decoupling between bulk quintuple layers with high Se vacancies)[30,31]. As seen in Fig. 4a, increasing T does not substantially weaken the QH states until at least ~10 K, and QH states are still observable up to 35 K, before disappearing above ~50 K. Figure 4b,c shows further quantitative analysis of the T-dependence of the QHE at $\nu=1$ (both surface filling zeroth LLs). The σ_{xx} (QH minimum) exhibits a thermally activated behaviour ($\propto\exp(-E_0/kT)$) at higher T (Fig. 4b), with an extracted activation gap $E_0\sim5.6\pm0.3$ meV, but drops more slowly with decreasing T at lower T. The E_0 value is notably smaller than the theoretical energy separation $v_F(2eB\hbar)^{1/2}\sim60$ meV between the zeroth and first LLs of ideal 2D Dirac fermions, for a typical Fermi velocity $v_F\sim3\times10^5$ m s^{-1} estimated from ARPES measurements (refs 23,26 and Supplementary Fig. 2). This could stem from both disorder-induced Landau level broadening (such an effect was also seen in graphene with similar mobility[32]) and a finite thickness (side surface) effect[33]. At even higher temperature (>50 K), the bulk conduction starts to become significant and possibly suppresses the QH states. The thermally induced change ΔR_{xy} ($=R_{xy}(T)-R_{xy}(4.5\text{ K})$) versus R_{xx} at $\nu=1$ follows an approximately linear relationship (with a slope of −0.18, Fig. 4c). The T-dependence behaviours observed in Fig. 4b,c are qualitatively similar to those of the previously studied integer QHE in 2DES (ref. 5).

Further discussions and conclusion

A well-developed 'half-integer' QHE was previously observed for Dirac fermions (four-fold degenerate with two spins and two valleys) in graphene[34,35], giving QHC $\sigma_{xy}=4(N+1/2)e^2/h$. A zero-gap HgTe quantum well was found to give a 2DES with single-valley Dirac fermions (thus considered '1/2-graphene', with two spins), and exhibit a well-defined QHE (ref. 36). However, the observed QHC (in units of e^2/h) takes consecutive integer values rather than odd integers only (as would be expected for two-fold degenerate Dirac fermions), because the external magnetic field gives a substantial Zeeman splitting between the two spins (due to the large g-factor in HgTe) in addition to the orbital LLs. In contrast, a TI surface contains only one species of Dirac fermions (a single non-degenerate Dirac cone, sometimes referred to a '1/4-graphene'), resulting in a QHC of $(N+1/2)e^2/h$. Two such degenerate surfaces (as in Fig. 3) contribute in parallel to give the observed $\sigma_{xy}=2(N+1/2)e^2/h$ (odd integer plateaux). The surface (top or bottom) index in our sample can be viewed as a pseudospin, which is not affected by an external B field. One can use a gate voltage (controlling the chemical potential difference between two surfaces and, thus, acting as a fictitious Zeeman field) to make the pseudospins degenerate (giving odd integers of QHC, Fig. 3) or non-degenerate (giving consecutive integers of QHC, Fig. 2), realizing a more tunable system.

Developing QH plateaux have been observed in 3D TI of strained HgTe films; however, the accompanying R_{xx} minima remained well above zero[18,19]. Suggested possible causes for the less well-developed QHE with substantial dissipation (nonzero R_{xx}) may include non-chiral conducting surface states on the side surfaces, bulk conducting states or misalignment between top and bottom surface QH states[18,19]. The well-quantized R_{xy} (and σ_{xy}) accompanied by vanishing R_{xx} (and σ_{xx}) observed in our samples not only reflect the highly clean and insulating bulk and good overlap between top and bottom surface QH states, but may also indicate that our side surface TSS has been gapped out to be non-conducting (noting the quantization energy gap for a ~100 nm thick side surface is ~70 K, above the temperatures where we observe the QHE; this gap can be further increased by any magnetic field component perpendicular to the side surface).

It has been pointed out that QH physics in the closed 2D surface (topologically equivalent to a sphere) of a 3D TI can present subtle aspects unprecedented in previously studied (non-TI based) QH systems. For example, interesting questions have been asked about the QH chiral edge current, believed to become a chiral side surface current, which is spin-helical and shared between the two 'half' QH states in the top and bottom surfaces in a TI slab such as our sample. Theories even differed on the observabilities of a well-developed QHE in standard transport measurements[33,37–39]. Our experimental data confirm that a well-defined QHE can be observed in multi-terminal TI Hall bars, and will provide important insights to understand the TSS QHE.

In contrast to the well-developed TSS QHE we observed when the top and bottom surfaces have the same carrier type (electrons), the QHE features seem very different and conspicuously not well-developed when the two surfaces have opposite carriers (Fig. 2, see also Supplementary Figs 7 and 11)—with only weakly developing plateau-like features in σ_{xy} and substantial σ_{xx} (but no obvious features in R_{xy} and R_{xx}). This might indicate dissipation arising from two surfaces contributing opposite QH edge chiralities. Such an interesting situation has not been well addressed in previous experiments or theories, and warrants further studies to understand the fate of edge states and QH transport in this case.

The intrinsic TI studied in this work, exhibiting surface-dominated conduction at temperatures as high as room temperature and a surface Dirac fermion QHE at temperatures as high as ~35 K, demonstrates some of the most salient hallmarks of TSS transport free from contamination or the complications of bulk conduction. This system could provide an excellent 'clean' experimental platform to pursue the plethora of exciting physics and applications proposed for ideal TIs, such as Majorana fermions and topological magnetoelectrics, when interfaced with superconducting or magnetic materials respectively.

Methods

Bulk single crystals of nominal composition $BiSbTeSe_2$ were grown by the vertical Bridgman technique from appropriately weighted starting materials in a two-zone high-temperature furnace. The value of the temperature profile in the growth zone was regulated by changing the distance between the heating zones. All the syntheses were performed in closed graphitized fused quartz ampoules evacuated for several hours, and sealed off under a dynamic vacuum of $\sim 10^{-8}$ torr. After a preliminary reaction at 400 °C, followed by a slow heating up to 770 °C for approximately 6 h, the melt was allowed to homogenize for 24 h under a high linear temperature gradient to promote mixing. The melt was solidified at a rate of about 1 mm h^{-1} with linear gradients of 20–50 °C cm^{-1}.

The crystal can be easily cleaved along the plane perpendicular to the c axis, and either fabricated into bulk devices (thickness $>$ 1 µm) with multiple indium contacts, or exfoliated (using Scotch tape) into thinner flakes (below 500 nm, with thicknesses measured by atomic force microscopy) placed on doped Si substrates coated with 300-nm-thick SiO_2. The Cr/Au electrodes for the devices on exfoliated flakes are defined by standard electron-beam lithography and metal evaporation.

Transport measurements were performed either in a variable temperature insert system, with a temperature variable between 1.6 K and 300 K in a magnetic field up to 6 T, or in a helium-3 system with base temperature down to 350 mK and magnetic fields up to 31 T (at the National High Magnetic Field Laboratory). Four-terminal longitudinal (R_{xx}) and Hall (R_{xy}) resistances were measured with the standard lock-in technique and a low-frequency (<20 Hz) excitation current of 100 nA. The corresponding 2D resistivities are $\rho_{xx}=R_{xx}\ (W/L)=R_{sh}$ (sheet resistance, where W and L are the channel width and length between the R_{xx} voltage probes of our quasi-Hall-bar devices) and $\rho_{xy}=R_{xy}$, and the conductivities are $\sigma_{xx}=\rho_{xx}/(\rho_{xx}{}^2+\rho_{xy}{}^2)$ and $\sigma_{xy}=\rho_{xy}/(\rho_{xx}{}^2+\rho_{xy}{}^2)$.

Received 15 June 2014; accepted 23 September 2014;

References

1. Klitzing, K. v., Dorda, G. & Pepper, M. New method for high-accuracy determination of the fine-structure constant based on quantized Hall resistance. *Phys. Rev. Lett.* **45,** 494–497 (1980).
2. Girvin, S. M. in *Topological Aspects of Low Dimensional Systems* (eds Comtet, A., Jolicoeur, T., Ouvry, S. & David, F.) (Springer, 2000).
3. Laughlin, R. B. Quantized Hall conductivity in two dimensions. *Phys. Rev. B* **23,** 5632–5633 (1981).
4. Thouless, D. J., Kohmoto, M., Nightingale, M. P. & den Nijs, M. Quantized Hall conductance in a two-dimensional periodic potential. *Phys. Rev. Lett.* **49,** 405–408 (1982).
5. Prange, R. E., Girvin, S. M. & Klitzing, K. v. (eds) *The Quantum Hall Effect* 2nd edn (Springer, 1989).
6. Hasan, M. Z. & Kane, C. L. Topological insulators. *Rev. Mod. Phys.* **82,** 3045–3067 (2010).
7. Qi, X. L. & Zhang, S. C. Topological insulators and superconductors. *Rev. Mod. Phys.* **83,** 1057–1110 (2011).
8. Fu, L. & Kane, C. L. Topological insulators with inversion symmetry. *Phys. Rev. B* **76,** 045302 (2007).
9. Qi, X. L., Hughes, T. L. & Zhang, S. C. Topological field theory of time-reversal invariant insulators. *Phys. Rev. B* **78,** 195424 (2008).
10. Liu, C. X., Qi, X. L., Dai, X., Fang, Z. & Zhang, S. C. Quantum anomalous Hall effect in $Hg_{1-y}Mn_yTe$ quantum wells. *Phys. Rev. Lett.* **101,** 146802 (2008).
11. Yu, R. *et al.* Quantized anomalous Hall effect in magnetic topological insulators. *Science* **329,** 61–64 (2010).
12. Chang, C. Z. *et al.* Experimental observation of the quantum anomalous Hall effect in a magnetic topological insulator. *Science* **340,** 167–170 (2013).
13. Analytis, J. G. *et al.* Two-dimensional surface state in the quantum limit of a topological insulator. *Nature Phys.* **6,** 960–964 (2010).
14. Qu, D. X., Hor, Y. S., Xiong, J., Cava, R. J. & Ong, N. P. Quantum oscillations and Hall anomaly of surface states in the topological insulator Bi_2Te_3. *Science* **329,** 821–824 (2010).
15. Ren, Z., Taskin, A. A., Sasaki, S., Segawa, K. & Ando, Y. Large bulk resistivity and surface quantum oscillations in the topological insulator Bi_2Te_2Se. *Phys. Rev. B* **82,** 241306 (2010).
16. Xiong, J., Petersen, A. C., Qu, D., Cava, R. J. & Ong, N. P. Quantum oscillations in a topological insulator Bi_2Te_2Se with large bulk resistivity (6 Ω cm). *Physica E* **44,** 917–920 (2012).
17. Taskin, A. A., Ren, Z., Sasaki, S., Segawa, K. & Ando, Y. Observation of Dirac holes and electrons in a topological insulator. *Phys. Rev. Lett.* **107,** 016801 (2011).
18. Brüne, C. *et al.* Quantum Hall effect from the topological surface states of strained bulk HgTe. *Phys. Rev. Lett.* **106,** 126803 (2011).
19. Kozlov, D. A. *et al.* Transport properties of a 3D topological insulator based on a strained high-mobility HgTe film. *Phys. Rev. Lett.* **112,** 196801 (2014).
20. Analytis, J. G. *et al.* Bulk Fermi surface coexistence with Dirac surface state in Bi_2Se_3: A comparison of photoemission and Shubnikov–de Haas measurements. *Phys. Rev. B* **81,** 205407 (2010).

21. Checkelsky, J. G., Hor, Y. S., Cava, R. J. & Ong, N. P. Bulk band gap and surface state conduction observed in voltage-tuned crystals of the topological insulator Bi_2Se_3. *Phys. Rev. Lett.* **106,** 196801 (2011).
22. Kim, D. *et al.* Surface conduction of topological Dirac electrons in bulk insulating Bi_2Se_3. *Nature Phys.* **8,** 459–463 (2012).
23. Arakane, T. *et al.* Tunable Dirac cone in the topological insulator $Bi_{2-x}Sb_xTe_{3-y}Se_y$. *Nature Commun.* **3,** 636 (2012).
24. Xia, B. *et al.* Indications of surface-dominated transport in single crystalline nanoflake devices of topological insulator $Bi_{1.5}Sb_{0.5}Te_{1.8}Se_{1.2}$. *Phys. Rev. B* **87,** 085442 (2013).
25. Segawa, K. *et al.* Ambipolar transport in bulk crystals of a topological insulator by gating with ionic liquid. *Phys. Rev. B* **86,** 075306 (2012).
26. Neupane, M. *et al.* Topological surface states and Dirac point tuning in ternary topological insulators. *Phys. Rev. B* **85,** 235406 (2012).
27. Gao, B. F. *et al.* Gate-controlled linear magnetoresistance in thin Bi_2Se_3 sheets. *Appl. Phys. Lett.* **100,** 212402 (2012).
28. Giraud, S., Kundu, A. & Egger, R. Electron–phonon scattering in topological insulator thin films. *Phys. Rev. B* **85,** 035441 (2012).
29. Skinner, B., Chen, T. & Shklovskii, B. I. Effects of bulk charged impurities on the bulk and surface transport in three-dimensional topological insulators. *J. Exp. Theor. Phys.* **117,** 579–592 (2013).
30. Cao, H. *et al.* Quantized Hall effect and Shubnikov–de Haas oscillations in highly doped Bi_2Se_3: Evidence for layered transport of bulk carriers. *Phys. Rev. Lett.* **108,** 216803 (2012).
31. Cao, H. *et al.* Structural and electronic properties of highly doped topological insulator Bi_2Se_3 crystals. *Phys. Status Solidi* **7,** 133–135 (2013).
32. Jabakhanji, B. *et al.* Tuning the transport properties of graphene films grown by CVD on SiC(0001): Effect of *in situ* hydrogenation and annealing. *Phys. Rev. B* **89,** 085422 (2014).
33. Zhang, Y. Y., Wang, X. R. & Xie, X. C. Three-dimensional topological insulator in a magnetic field: Chiral side surface states and quantized Hall conductance. *J. Phys. Condens. Matter* **24,** 015004 (2012).
34. Novoselov, K. S. *et al.* Two-dimensional gas of massless Dirac fermions in graphene. *Nature* **438,** 197–200 (2005).
35. Zhang, Y. *et al.* Experimental observation of the quantum Hall effect and Berry's phase in graphene. *Nature* **438,** 201–204 (2005).
36. Büttner, B. *et al.* Single valley Dirac fermions in zero-gap HgTe quantum wells. *Nature Phys.* **7,** 418–422 (2011).
37. Lee, D. H. Surface states of topological insulators: The Dirac fermion in curved two-dimensional spaces. *Phys. Rev. Lett.* **103,** 196804 (2009).
38. Chu, R. L., Shi, J. & Shen, S. Q. Surface edge state and half-quantized Hall conductance in topological insulators. *Phys. Rev. B* **84,** 085312 (2011).
39. Vafek, O. Quantum Hall effect in a singly and doubly connected three-dimensional topological insulator. *Phys. Rev. B* **84,** 245417 (2011).

Acknowledgements

We acknowledge support from DARPA MESO program (Grant N66001-11-1-4107). H.N. and C-K.S. acknowledge support from the Welch Foundation (Grant F-1672) and ARO (Grants W911NF-09-1-0527 and W911NF-12-1-0308). High magnetic field transport measurements were performed at the National High Magnetic Field Laboratory (NHMFL), which is jointly supported by the National Science Foundation (DMR0654118) and the State of Florida. We thank E. Palm, T. Murphy, J. Jaroszynski, E. Sang, H. Cao, J. Coy and T. Wu for experimental assistance.

Author contributions

Y.P.C. supervised the research. I.M. synthesized the crystals. Y.X. characterized the materials, fabricated the devices, performed the transport measurements, and analysed the data. J.T. performed EDX characterization. C.L., N.A. and M.Z.H. performed ARPES characterization. H.N. and C-K.S. performed STS characterization. J.H. assisted the transport measurements. Y.P.C. and Y.X. wrote the paper, with comments from other co-authors.

Additional information

Supplementary information is available in the online version of the paper. Reprints and permissions information is available online at www.nature.com/reprints. Correspondence and requests for materials should be addressed to Y.P.C.

Competing financial interests

The authors declare no competing financial interests.